Geophysical Research Letters

RESEARCH LETTER
10.1029/2020GL088147

**Key Points:**
- The reconnection rate and outflow speed in 3-D reconnection with a limited x-line extent are quantitatively modeled
- The key length scale of the suppression region $\simeq 10d_i$ due to the flux transport by electrons is incorporated to develop our models
- The phase shift between the **J** and **B** profiles at the outflow region reduces the outflow speed in the short x-line limit

**Correspondence to:**
K. Huang,
inhk@mail.ustc.edu.cn

**Citation:**
Huang, K., Liu, Y.-H., Lu, Q., & Hesse, M. (2020). Scaling of magnetic reconnection with a limited x-line extent. *Geophysical Research Letters*, *47*, e2020GL088147. https://doi.org/10.1029/2020GL088147

Received 27 MAR 2020
Accepted 7 SEP 2020
Accepted article online 14 SEP 2020



# Scaling of Magnetic Reconnection With a Limited X-Line Extent

**Kai Huang[1,2,3], Yi-Hsin Liu[3], Quanming Lu[1,2], and Michael Hesse[4]**

[1]CAS Key Laboratory of Geospace Environment, School of Earth and Space Sciences, University of Science and Technology of China, Hefei, China, [2]CAS Center for Excellence in Comparative Planetology, Hefei, China, [3]Department of Physics and Astronomy, Dartmouth College, Hanover, NH, USA, [4]Department of Physics and Technology, University of Bergen, Bergen, Norway

**Abstract** Contrary to all the 2-D models, where the reconnection x-line extent is infinitely long, we study magnetic reconnection in the opposite limit. An internal x-line asymmetry along the current direction develops because of the transport of reconnected magnetic flux by electrons beneath the ion kinetic scale, resulting in a suppression region identified in Liu et al. (2019, https://doi.org/10.1029/2019JA026539). In this letter, we incorporate the length scale of this suppression region $\simeq 10d_i$ to quantitatively model the reduction of the reconnection rate and the maximum outflow speed observed in the short x-line limit. The average reconnection rate drops because of the limited active region (where the current sheet thins down to the electron inertial scale) within an x-line. The outflow speed reduction correlates with the decrease of the $\mathbf{J}\times\mathbf{B}$ force, that can be modeled by the phase shift between the **J** and **B** profiles, also as a consequence of the flux transport.

**Plain Language Summary** Magnetic reconnection is a fundamental physical process that is responsible for releasing the magnetic energy during substorms of planetary magnetotails. Previous studies of magnetic reconnection usually take the two-dimensional (2-D) approach, which assumes that reconnection is uniform in the third direction out of the 2-D reconnection plane. However, observations suggest that reconnection can be limited in the third direction, such as reconnection at Mercury's magnetotail. It turns out that reconnection can be suppressed when reconnection region is very limited in the third direction. Under the guidance of a series of 3-D kinetic simulations, in this work, we write down quantitative models to describe how the reconnection rate and reconnection outflow speed drop in this limit. Notably, these two quantities are most essential in defining the well-being of magnetic reconnection, which can tell us when reconnection shall be suppressed. The models are formulated by considering the transport of reconnected magnetic flux in the third direction, which can weaken the driver of the reconnection process.

## 1. Introduction

Magnetic reconnection can explosively release the magnetic energy when the magnetic geometry develops antiparallel components to host a thin current sheet. It plays a critical role in planetary magnetospheres (Angelopoulos et al., 2008; Dungey, 1961), solar wind (Gosling et al., 2005; Phan et al., 2006), solar flares (Giovanelli, 1946; Masuda et al., 1994), and potentially in astrophysical systems (Uzdensky, 2011; Zweibel & Yamada, 2009). The basic idea of magnetic reconnection can be captured in a "two-dimensional (2-D)" picture, that involves the break and rejoining of magnetic field lines on a 2-D plane. However, 2-D models and simulations of magnetic reconnection enforces quantities to be translational invariant in the out-of-plane direction. Consequentially, reconnection x-line is *infinitely* long. The same situation also carries over to most three-dimensional (3-D) simulations that have a uniform initial current sheet and periodic boundary condition in the x-line direction. While results from 2-D models are sufficient as long as the spatial and temporal scales of the variation along the x-line are large (e.g., Genestreti et al., 2018; Nakamura, Genestreti, Liu, et al., 2018; Nakamura, Genestreti, Nakamura, et al. 2018; Tobert et al., 2018), some incidences (Shay et al., 2003; Zou et al., 2020) suggest that reconnection is operating in the opposite limit, and its property is far less understood.

Observations and simulations indicate that the reconnection x-line can be spatially confined. For instance, in the magnetotails of planets (e.g., Mercury) (Chen et al., 2019; Dong et al., 2019; Rong et al., 2018; Slavin

et al., 2009), moons (e.g., Ganymede) (Dorelli et al., 2015), and comets (Russell et al., 1986), the spatial scale in the cross-tail (i.e., x-line) direction is comparable to the plasma kinetic scale. Even in planets with a larger magnetotail, like Earth, the onset of magnetic reconnection may occur within a spatially limited thin current sheet; the spatial scale may be determined by the size of external drivers (Nishimura & Lyons, 2016), the wavelength of cross-tail instabilities (Pritchett & Coroniti, 2011; Pritchett et al., 2014), or the inhomogeneity of the neutral sheet caused by other global effects (Baker et al., 1982). The resulting spatially confined reconnection could be relevant to the generation of dipolarizing flux bundles (DFBs) (Liu, Angelopoulos, et al., 2015), or bursty bulk flows (BBFs) (Nakamura et al., 2004; Nagai et al., 2013), that have short cross-tail extents. In Earth's magnetosheath downstream of a quasi-parallel shock, the lengths of the flux ropes generated by reconnection can also be as short as several Earth's radii (Lu et al., 2020). Thus reconnection with a limited x-line extent can be ubiquitous, and it is imperative to study its nature.

Using 3-D particle-in-cell simulations, Liu et al. (2019) studied the internal x-line asymmetry during reconnection with a limited x-line extent. The initial condition is a modified Harris sheet with varying thickness along the current direction. Thick current sheets are employed on the two ends of a thin current to prevent the x-line from spreading (Li et al., 2020; Nakamura et al., 2012; Shepherd & Cassak, 2012); reconnection is thus confined within the thin current sheet. It is found that on the electron-drifting side, there is an active region where reconnection process as in 2-D models, while on the ion-drifting side, reconnection is suppressed. This internal x-line asymmetry develops because the reconnected flux is transported to the electron-drifting side. The suppression region length scale $L_{supp} \simeq \mathcal{O}(10d_i)$ along the x-line direction is estimated by multiplying the electron drift speed to the time scale of current sheet thinning (that leads to fast reconnection). This suppression region scale may reverse the dawn-dusk asymmetry observed at Mercury's magnetotail, that has a global cross-tail extent ≃20–50 $d_i$ (Liu et al., 2019; Sun et al., 2016). They also found that reconnection rate and outflow speed drop significantly when x-line is shorter than $\simeq \mathcal{O}(10d_i)$. However, a quantitative model that describes this drop was not derived. Knowing the detailed scaling of reconnection in the short x-line limit is especially important because in situ measurements indicate that the typical cross-tail extent of DFBs observed at Earth's magnetotail is less than $3R_E \simeq 60d_i$ while the shortest extent is $\simeq 0.5R_E \simeq 10d_i$ (Liu, Angelopoulos, et al. 2015). Reconnection x-lines localized in the cross-tail direction could be a potential source of these narrow DFBs.

In this letter, we quantitatively model the reconnection rates and ion outflow speeds as a function of the x-line extent after incorporating the intrinsic length-scale of suppression region $L_{supp} \simeq \mathcal{O}(10d_i)$ (Liu et al., 2019). Through a parametrical study of 3-D reconnection simulations with different x-line extents, we unravel several key details. We find that the active region only forms when the current sheet thins down to the electron inertial ($d_e$) scale, where a local fast rate of order 0.1 is hosted; this indicates the importance of the breaking of electron frozen-in condition. The average reconnection rate can be well estimated using the ratio between the active region extent and the entire x-line. While reconnection outflows are driven by the $\mathbf{J}\times\mathbf{B}$ force, it can decreases due to the phase shift between the $B_z$ and $J_y$ profiles at the outflow region. The similar trend of the outflow and rate reductions suggest that the development of reconnection outflows correlates with the current sheet thinning, that enables the development of a $d_e$-scale thin active region.

## 2. Simulation Setup

We use the particle-in-cell code VPIC (Bowers, Albright, Bergen, et al., 2008; Bowers, Albright, Yin, et al., 2008; Bowers et al., 2009) to produce simulations. The initial condition is the same as Liu et al. (2019) that has a modified Harris sheet with magnetic field $\mathbf{B}(y,z) = B_0 \tanh[z/L(y)]\mathbf{e}_x$ and plasma density $n(y,z) = n_0 \operatorname{sech}^2[z/L(y)] + n_b$, where $L(y) = L_{min} + (L_{max} - L_{min})[1 - f(y)]$ is the half thickness of the current sheet, and $f(y) = [\tanh((y + w_0)/S) - \tanh((y - w_0)/S)]/[2\tanh(w_0/S)]$. Here, $B_0$ is the asymptotic value of reconnecting magnetic field and $n_0$ is the peak density of the Harris sheet. In the simulations, $L_{min} = 0.5d_i$, $L_{max} = 4d_i$, and $S = 5d_i$. The $n_b = 0.3n_0$ is the background density. In this setup a thin current sheet of thickness $1d_i$ is embedded between thick current sheets of thickness $8d_i$. Reconnection proceeds with a limited x-line extent that does not spread into the thick sheets (Liu et al., 2019). Ion drift velocity $V_{iy}$ is kept constant along the $y$ direction, while $V_{ey}$, $T_i$, and $T_e$ vary to satisfy the Ampere's law and $-V_{iy}/V_{ey} = T_i/T_e$. In the thick current sheets, the temperature ratio between ion and electron is $T_i/T_e = 5$. Here $d_i = c(\varepsilon_0 m_i/n_0 e^2)^{1/2}$ is the ion inertial length. The length of the thin current sheet $L_{y,thin}$ (i.e., the x-line extent) is defined as the region with $L < 1d_i$, which is a free parameter controlled by varying $w_0$. The characteristic Alfvén speed is $V_A \equiv B_0/(\mu_0 m_i n_0)^{1/2}$ and ion gyrofrequency is $\Omega_i \equiv eB_0/m_i$, where the ion to electron

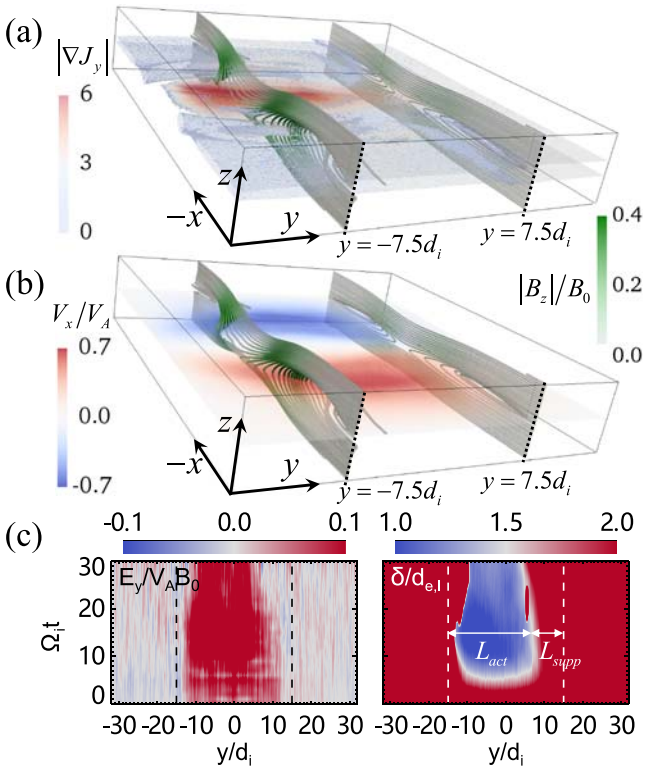


**Figure 1.** The representative 3-D structure of the internal x-line asymmetry in the $L_{y,thin} = 30d_i$ case at time $15/\Omega_i$. The domain shown here is $[-16, 16] \times [-15, 15] \times [-3, 3]d_i$. (a) The isosurface of the current density $J_y$ colored by its gradient $|\nabla J_y|$. Sample magnetic field lines tracing from $x, y = (\pm 16, \pm 7.5)d_i$ are colored by the magnitude of $|B_z|$. (b) Ion outflow speed $V_x$ on the $z = 0$ plane. (c) Time stacks of the reconnection electric field $E_y$ and the currents sheet half-thickness $\delta$ along the x-line. The extent of the x-line is controlled by $L_{y,thin}$, that is bounded between the two vertical dashed lines. It consist of an active region with extent $L_{act}$, and the suppression region with extent $L_{supp} = L_{y,thin} - L_{act}$.

mass ratio $m_i/m_e = 25$ is used. In these simulations, light speed is $c = 20V_A$ and the upstream plasma $\beta = 0.3$. Initial perturbation $\delta B_z = 0.05B_0$ is used to induce reconnection. Simulations are performed within boxes of size $L_x \times L_y \times L_z = 32d_i \times 64d_i \times 16d_i$ and $640 \times 1{,}280 \times 320$ cells. Over $2.6 \times 10^{10}$ particles for each species are used in the simulations. The boundary conditions are periodic in the $x$ and $y$ directions, while in the $z$ direction they are conducting for fields and reflecting for particles.

## 3. Overview of the Internal X-Line Asymmetry

Figure 1 displays the morphology of magnetic reconnection with a limited x-line extent $L_{y,thin} = 30d_i$ in the $y$ direction. Figure 1a shows the isosurface of the current density $J_y$ that is colored by $|\nabla J_y|$. In the reddish region, the current sheet is thinner. Figure 1b shows the ion outflow speed $V_x$ on the $z = 0$ plane. It is clear that the active region with a thinner current sheet and large ion outflow speeds appear on the electron-drifting side ($-y$ direction), while on the ion-drifting side ($+y$ direction) the reconnection is suppressed. We refer this as the "internal x-line asymmetry" hereafter. The 3-D magnetic field lines across the active region at $y \simeq -7.5d_i$ and the suppression region at $y \simeq 7.5d_i$ are plotted with the color showing the local strength of $B_z$. This internal x-line asymmetry develops because $B_z$ is transported to the electron-drifting side by the electron diamagnetic and $\mathbf{E} \times \mathbf{B}$ drifts (Liu et al., 2019; Liu & Hesse, 2016). In this letter, we will quantitatively model how this magnetic flux transport affects the reconnection rate and outflow speed.

It has been demonstrated that the thickness of the electron diffusion region during fast reconnection is on the electron inertia scale (Huang, Lu, Yang, et al., 2011; Huang, Lu, Gao, et al., 2018; Ji et al., 1998; Olson et al., 2016; Wygant et al., 2005), thus we trace the active region of the x-line using criterion $\delta < 2d_{e,l}$, that is triggered when the current sheet half-thickness is thinner than two local electron inertial length. Figure 1c shows the time stacks of the reconnection electric field $E_y$ and the current sheet half-thickness $\delta$ along the

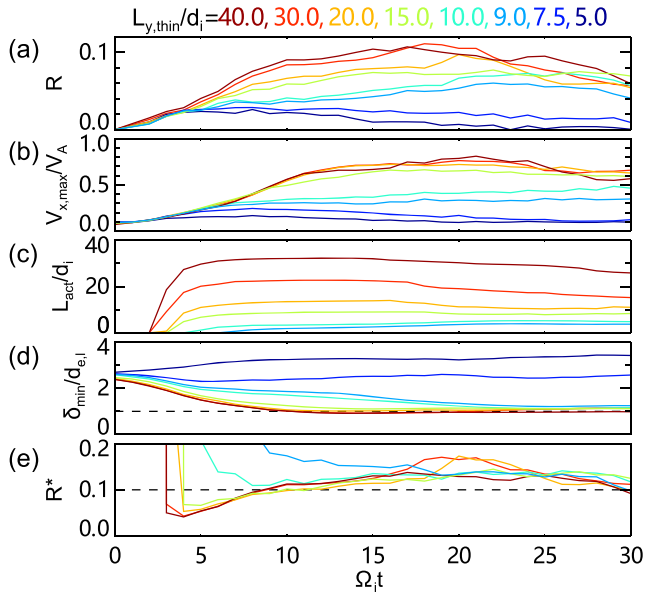


**Figure 2.** Time evolution of (a) the average reconnection rate $R$, (b) the maximum ion outflow speed $V_{x,max}$, (c) the active region extent $L_{act}$, (d) the minimum half-thickness of the current sheet $\delta_{min}$, and (e) the reconnection rate normalized by the active region extent $R^*$. Cases with $L_{y,thin}/d_i$ = 40, 30, 20, 15, 10, 9, 7.5, and 5 are shown in different colors. The $L_{y,thin}/d_i$ = 7.5 and 5 cases are not shown in (c) and (e) because of lacking an active region.

x-line; here we use $J_y$ to calculate $\delta$. We can see that the active ($\delta < 2d_{e,l}$) region in blue coincides with the region with large $E_y$ region in red. The local $E_y$ reaching the typical fast rate value $\simeq 0.1 V_A B_0$ (Birn et al., 2001; Cassak et al., 2017; Genestreti et al., 2018; Liu et al., 2017; Nakamura, Genestreti, Liu, et al., 2018; Shay & Drake, 1998). The thin current sheet consists of two distinct regions: the active region of extent $L_{act}$ and the suppression region of extent $L_{supp}$; thus, $L_{y,thin} = L_{act} + L_{supp}$ as shown in Figure 1c. The observed suppression region extent $L_{supp} \simeq 10d_i$ is consistent with that reported in Liu et al. (2019), which was explained using the multiplication of the current sheet thinning time-scale and the electron drift speed.

## 4. Modeling of Reconnection Rate

The time evolution of important quantities in all the cases are given in Figure 2. Panels (a) and (b) show the average reconnection rates $R$ and maximum ion outflow speeds $V_{x,max}$, respectively. Here $R \equiv \partial_t \Psi / (V_A B_0 L_{y,thin})$, where $\Psi = -\int_{-L_y/2}^{L_y/2} \int_{-L_x/2}^{X(y)} B_z(x, y, 0) \mathrm{d}x \mathrm{d}y$ is the reconnected flux and $X(y)$ is the location of the primary x-line that maximizes $\Psi(X) = -\int_{-L_x/2}^{X} B_z(x, y, 0) \mathrm{d}x$ at a given $y$. Note that the current sheet is symmetric with respect to the $z = 0$ plane, $B_z$ at $z = 0$ will thus be the reconnected flux. It is evident that both reconnection rates and ion outflow speeds decrease when $L_{y,thin}$ become shorter and are strongly suppressed when $L_{y,thin}$ is shorter than $\simeq 10d_i$. Figures 2c and 2d show the time evolution of the active region extent $L_{act}$ and the minimum current sheet half-thickness $\delta_{min}$, respectively. For the $L_{y,thin} > 10d_i$ cases, a quasi-steady active region exists and $\delta_{min}$ clearly reaches the local electron inertial length $d_{e,l}$. For the two cases with $L_{y,thin} < L_{supp} \simeq 10d_i$, there is no active region, indicating that the current sheet does not thin much. It is clear that the current sheet thinning is important in facilitating fast reconnection in these simulations, and the critical thickness is the local electron inertial length $d_{e,l}$ where the electron frozen-in condition can be violated.

In Figure 2e, we renormalize the reconnection rate by the active region extent, $R^* \equiv \partial_t \Psi / (V_A B_0 L_{act})$. Surprisingly, cases with an active region all appear to have a similar rate $R^* \simeq \mathcal{O}(0.1)$. In light of this observation, we model the averaged reconnection rate as

$$R = \frac{L_{act}}{L_{y,thin}} R^* \simeq \left(1 - \frac{L_{supp}}{L_{y,thin}}\right) R^* \tag{1}$$

where $L_{supp} \simeq \mathcal{O}(10d_i)$ (Liu et al., 2019). Note that Equation 1 cannot explain the small reconnection rate observed in the $L_{y,thin}/d_i$ = 7.5 and 5 cases; the short transient reconnecting period (Figure 2a) arises

from the initial perturbation, but it tapers off quickly before being affected by the boundary. For the case with $L_{y,thin} = 9d_i$ (the blue line in Figure 2e), $R^*$ appears to be larger because an active region of $d_e$-scale thin becomes harder to form when $L_{y,thin}$ is closer to the critical value $\simeq 10d_i$, resulting in a systematically shorter $L_{act}$ for a prolonged transient phase; $R^*$ (which is normalized by $L_{act}$) thus appears to be larger before reaching the quasi-steady state.

## 5. Modeling of the Outflow Speed

To model the ion outflow speed, we analyze the momentum equation, $m_i[\partial_t(n\mathbf{V}) + \nabla\cdot(n\mathbf{VV})] = \mathbf{J}\times\mathbf{B} - \nabla\cdot\mathbf{P}$. Here $\mathbf{V}$ is the ion velocity, $\mathbf{J}$ is the total current density, and $\mathbf{P}$ is the total pressure tensor. It is important to realize that only the $\mathbf{J}\times\mathbf{B}$ force is the driver of reconnection outflows. While gaining the bulk speed, outflowing plasmas are also heated, developing a pressure gradient to hinder the acceleration. Previous studies suggest that ions gain thermal energy when they are picked up by the outflow magnetic fields (Drake et al., 2009), resulting in an effective thermal velocity equal to the outflow speed; the temperature increase along the outflow can thus be modeled as $\Delta T_i \propto m_i V_{out}^2$. For these reasons, we absorb the pressure gradient into the inertial term by assuming, $\nabla\cdot\mathbf{P} \propto m_i\nabla\cdot(n\mathbf{VV})$, and it only makes a constant correction. Considering the quasi-steady state, then the $\partial/\partial t$ term is negligible. These greatly simplify the force balance on the $z = 0$ plane into

$$\partial_x(nV_xV_x) + \partial_y(nV_yV_x) \propto J_yB_z. \tag{2}$$

Note that the $\partial_z(nV_zV_x)$ term is also found to be much smaller in the region where the outflow is accelerated.

By balancing the first term of the left-hand side (LHS) to the right-hand side (RHS), we recover the Alfvénic outflow speed (Parker, 1957). The second term of LHS has some effect at the edges, but it is the transport of $B_z$ that significantly reduces $J_yB_z$ on RHS, and thus the outflow speed in small $L_{y,thin}$ cases, as we will see. Figure 3a shows the three terms of Equation 2 in the case of $L_{y,thin} = 30d_i$. Note that the x-line is along the $x = 0$ axis and only the outflow exhaust at $x > 0$ are shown in Figure 3a. The average of these terms over $0 < x < \xi$ are plotted in panel (b); here $x = \xi$ is the position (indicated by the vertical dashed line in panel (a)) where $V_x$ reaches the maximum. The averaged functions is defined as $F(y) = \int_0^\xi f(x,y)\mathrm{d}x/\xi$. In addition to the $L_{y,thin} = 30d_i$ case, we also show cases with $L_{y,thin} = 10d_i$ and $7.5d_i$; these three cases represent systems with a "long active region," "short active region," and "no active region," respectively. In all three cases, $F(y)$ is normalized by the maximum of $J_yB_z$, so that we can compare the ratio between the inertia terms and the $\mathbf{J}\times\mathbf{B}$ force term. The total inertia (in green) is roughly 30% of $J_yB_z$ in all three cases, and this justifies the proportionality when absorbing $\nabla\cdot\mathbf{P}$ in the inertial term; that is, this result also indicates that the pickup mechanism is valid in our simulations, although 2-D condition is used in Drake et al. (2009). Note that an additional factor of 0.3 gives us an outflow speed $\sim 0.55V_A$, which is still considered Alfvénic and this is, in fact, often seen in 2-D kinetic simulations. We have also checked that the $\partial/\partial t$ term at the time frames of panel (b) is small compared with other terms, indicating that the quasi-steady assumption is valid. The dominant inertial term is $\partial_x(nV_xV_x)$, while $\partial_y(nV_yV_x)$ only becomes nonnegligible at the edge of outflows in cases with a short $L_{y,thin}$. If the $\partial_y(nV_yV_x)$ term controls the internal x-line asymmetry, it should cause a suppression region on the electron-drifting side instead (Arnold et al., 2018), but this is not seen in our simulations. For these reasons, we further simplify Equation 2 to $V_x^2 \propto J_yB_z$ to model the relation between the ion outflow speed and its driver, $\mathbf{J}\times\mathbf{B}$ force, hereafter.

The peak values of $J_yB_z$ in these three cases are 0.283, 0.124, and 0.083, and this decrease is due to the phase shift between $J_y$ and $B_z$ when $B_z$ is transported away from the suppression region by electrons (i.e., a Hall effect). To illustrate this effect, we plot the averaged $J_y$ and $B_z$ in Figure 3c. The current density $J_y$ correlates with the thickness of the currents sheet, which remains close to the initial value from a $d_i$-scale sheet at the outflow region. The reconnected magnetic field $B_z$ at outflow also appears to be similar in all cases, likely limited by the upstream force balance (Liu et al., 2017). Thus, the peak values of $J_y$ ($B_z$) are considered similar in all three cases. However, while the peak of $J_y$ is located close to the center of the current sheet, the peak of $B_z$ is transported to the $-y$ direction. With a shorter $L_{y,thin}$, this phase shift becomes significant in reducing the $\mathbf{J}\times\mathbf{B}$ force. This transport distance is basically the suppression region extent $L_{supp}$, and it is gray-shaded in Figure 3c. Note that in the thick current sheet region (i.e., outside of the region between vertical dashed lines in (c)), $B_z$ decrease quickly because the electron drift speed is low in this region and $B_z$ will not be transported farther; also, $B_z$ in the $L_{y,thin} = 7.5d_i$ case mostly comes from the initial perturbation.

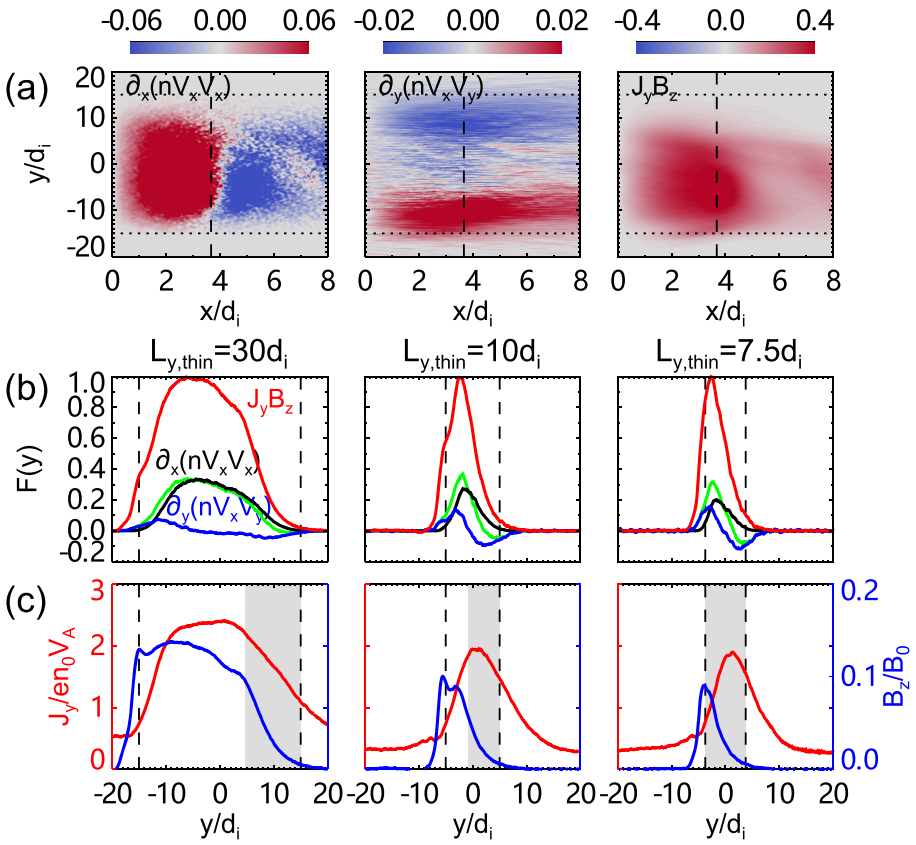


**Figure 3.** (a) The three terms in Equation 2 colored by their amplitude at the $z = 0$ plane in the $L_{y,thin} = 30d_i$ case, the horizontal dotted lines bound the thin current sheet, the vertical dashed lines is the location ($x = \xi$) where $V_x$ reaches the peak. (b) $\partial_x(nV_xV_x)$ in black, $\partial_y(nV_yV_x)$ in blue, $\partial_x(nV_xV_x) + \partial_y(nV_yV_x)$ in green, and $J_yB_z$ in red averaged over $0 < x < \xi$ in the cases with $L_{y,thin}/d_i = 30$, 10, and 7.5. Quantities are normalized by the maximum of $J_yB_z$ in each case. (c) $J_y$ in red and $B_z$ in blue averaged over $0 < x < \xi$. The gray-shaded region indicates the suppression region. The vertical dashed lines in (b) and (c) bound the thin current sheet region.

Motivated by these observations, we model the reduction of the $\mathbf{J} \times \mathbf{B}$ force in Figure 4. For simplicity, we assume that both $B_z$ and $J_y$ have the same functional form $f(y)$ that has a trapezium shape with a plateau in the center and transition regions of scale $L_{trans}$ on both flanks. During reconnection, $J_y$ at the outflow region is centered within the thin current sheet, but $B_z$ is transported to the $-y$ direction by distance $L_{supp}$. Thus $J_y = J_{y,max}f(y)$ and $B_z = B_{z,max}f(y + L_{supp})$. If $L_{act} \geq 2L_{trans}$ as in Figure 4a, part of the plateau regions of $J_y$ and $B_z$ overlap; therefore, $J_yB_z$ can reach the maximum value $J_{y,max}B_{z,max}$ and drives Alfvénic outflows with speed $\simeq V_A$. In contrast, if $L_{act} < 2L_{trans}$ as in panel (b), the plateau regions of $J_y$ and $B_z$ do not overlap. With this trapezium shape, $J_yB_z$ will reach the maximum at where $f(y) = f(y + L_{supp})$. Using the linear interpolation, we obtain $(J_yB_z)_{max} = (L_{act}/2L_{trans})^2 J_{y,max}B_{z,max}$. Combined with $V_x^2 \propto J_yB_z$ we model the reconnection outflow speed as

$$V_{x,max} = \begin{cases} V_m \simeq V_A & \text{if } L_{act} \geq 2L_{trans} \\ (L_{act}/2L_{trans})V_m & \text{otherwise.} \end{cases} \quad (3)$$

where $L_{act} = L_{y,thin} - L_{supp}$. The maximum reconnection outflow speed scales linearly with the $y$ extent of the active region in the short x-line limit. When the active region is absent, the reconnection outflow should be totally suppressed, as expected. Liu et al. (2019) only intuitively argued that reconnection shall be suppressed if the x-line extent $L_{y,thin}$ is shorter than the suppression region extent $L_{supp}$. In this work, we analyze the momentum equation in great details to show that this $L_{supp}$ causes the phase shift between $\mathbf{J}$ and $\mathbf{B}$, which weakens the driver of reconnection outflows.

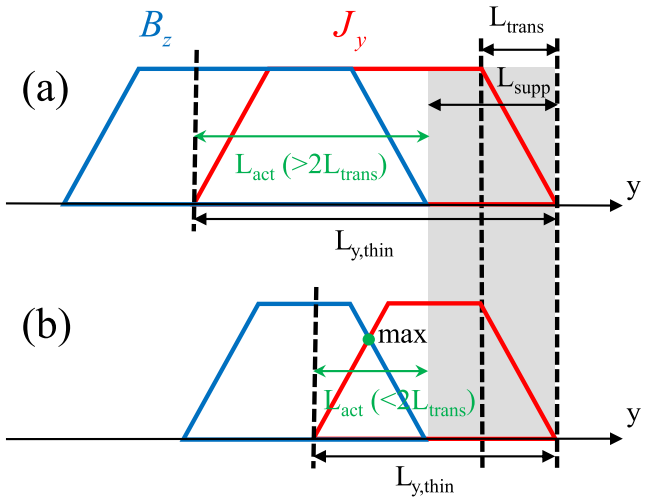


**Figure 4.** Modeling the reduction of $J_yB_z$ that results from the phase shift between the $B_z$ and $J_y$ profiles. Panel (a) has $L_{act} > 2L_{trans}$, while panel (b) has $L_{act} < 2L_{trans}$. Colors are designed to match those in Figure 3c.

## 6. Model-Data Comparison and Remarks

In this letter, we provide quantitative models for the reconnection rate (Equation 1) and outflow speed (Equation 3) of 3-D magnetic reconnection with a spatially confined x-line extent. We summarize the simulation data and compare them with our models in Figure 5. Panel (a) shows the time-averaged suppression region extent in all cases. For the $L_{y,thin}/d_i = 7.5$ and 5 cases, there is no active region so $L_{supp} = L_{y,thin}$. The red vertical segments are the error bars resulting from the time variation of $L_{supp}$. In all cases, $L_{supp}$ appears to be on the order of $10d_i$, consistent with Liu et al. (2019). Figure 5b plots the maximum reconnection rate $R$, and the solid curve is the prediction from Equation 1, where $R^*$ is set to be 0.15, and $L_{supp}$ uses the linear fit (dashed line) in Figure 5a. This curve traces the simulation results well. In panel (c), we plot the maximum ion outflow speed, and the solid curve is the prediction from Equation 3, where we use $V_m = 0.75V_A$, $L_{trans} = 4d_i$ estimated from the simulation results, $L_{act} = L_{y,thin} - L_{supp}$ with $L_{supp}$ again being the linear fit in Figure 5a. The model can explain most of the simulation result. The discrepancy is larger in the limit of smaller $L_{y,thin}$ where the active region is absent, likely because that nonvanishing transient outflows develop from the initial perturbation $\delta B_z$, such as the $L_{y,thin} = 7.5d_i$ case in Figure 3c.

In general, $R^* \sim \mathcal{O}(0.1)$, $V_m \sim \mathcal{O}(V_A)$ and $L_{supp} \sim \mathcal{O}(10d_i)$ can be used in our models, while $L_{trans}$ relates to the formation process of the thin current sheet; in Earth's magnetotail, possibilities include the wavelength

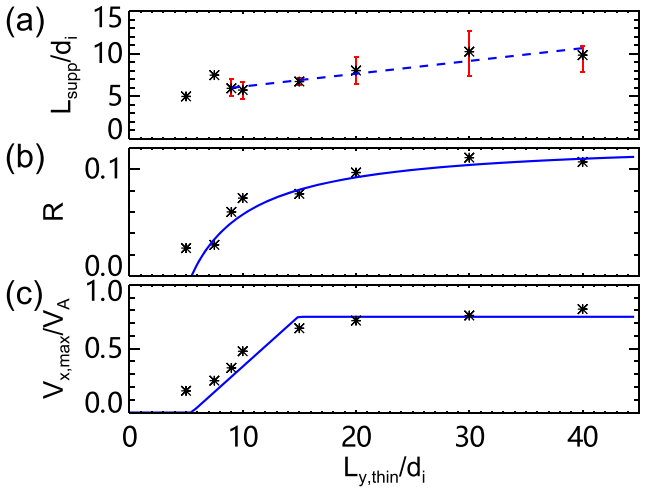


**Figure 5.** A comparison between the models (blue curves) and the simulation data (*). $L_{supp}$ in (a), $R$ in (b), and $V_{x,max}$ in (c).

of ballooning instability (Pritchett & Coroniti, 2011; Pritchett et al., 2014), or the size of localized streamers (Nishimura & Lyons, 2016) that triggers reconnection. From Figures 5b and 5c, $R$ and $V_{x,max}$ do appear to correlate with each other. In our simple model (Figure 4), outflows should not develop if $L_{y,thin}$ is smaller than $L_{supp}$, because $B_z$ is completely transported away from the suppression region (by definition). Thus, no reconnection is expected ($R = 0$), consistent with Equation 1. On the other hand, the opposite limit with $L_{y,thin} \gg L_{supp}$ recovers the 2-D result, as also expected. Intuitively, one may argue that $R \sim 0.1 \times (V_{x,max}/V_A)$ (i.e., here 0.1 is the typical fast rate observed in 2-D systems) and attribute the drop of the average rate solely to the reduction of the peak outflow speed. However, due to the complexity of such short 3-D x-line, other than this apparent correlation shown in Figure 5, we were not able to rigorously and explicitly establish the relation between $R$ and $V_{x,max}$.

In our study, the key to reduce both reconnection rate and outflow speed is the Hall effect, that allows drifting-electrons transport reconnected magnetic flux in the anticurrent direction. In particular, this transport causes the phase shift between the **J** and **B** profiles, reducing the driver of reconnection (i.e., the $\mathbf{J} \times \mathbf{B}$ force). In comparison, Meyer (2015) also studied the outflow reduction using 3-D two-fluid simulations. They argued that the turning of ion flows on the ion-drifting side of the diffusion region makes the $y$ extent of the outflow region longer than the $y$ extent of the inflow region, resulting in a lower energy gain in the outflow. Electron dynamics and the Hall effect, which are essential in our study, were not considered in their model. A future work is required to reconcile the difference. We expect that this suppression mechanism from the Hall effect will persist even with the existence of a guide field or with a different plasma $\beta$. However, additional simulations and analyses need to be performed to gain a quantitative model, since a higher $\beta$ or guide field may change the force balance. In addition, the development of oblique tearing modes and flux ropes during guide field reconnection (Daughton et al., 2011; Liu et al., 2013; Liu, Hesse, et al., 2018) could complicates the transport of reconnected magnetic flux.

Nevertheless, the primary application that motivates this study is Earth's magnetotail that has a relatively weak guide field. In addition to the application to DBFs/BBFs at Earth's magnetotail, our results also indicate that the energy release during substorms (i.e., tail reconnection) can be significantly affected by the cross-tail size of the magnetotail. If a planetary magnetosphere is too small (in terms of ion kinetic scales), substorms may be difficult to occur. These new results, such as the relation between the $B_z$ transport and outflow speed reduction, can be measured by the on-going ESA-JAXA mission, BepiColombo (van Casteren et al., 2010), that plans to map out the magnetic structure of Mercury's magnetosphere.

## Data Availability Statement

The data sets and scripts used to make the plots of this paper can be found at the Zenodo (http://doi.org/10.5281/zenodo.3922196).

**Acknowledgments**
This work was supported by the Strategic Priority Research Program of Chinese Academy of Sciences, Grant XDB 41000000 and the NSFC Grant 41527804, 41774169. Y. L. is grateful for support from NASA Grant 80NSSC18K0754 and MMS mission 80NSSC18K0289. M. H. is grateful for support from NASA' contract NNG04EB99C and Norwegian Research Council: 300865. Simulations were performed at National Energy Research Scientific Computing Center (NERSC).

## References

Angelopoulos, V., McFadden, J. P., Larson, D., Carlson, C. W., Mende, S. B., Frey, H., et al. (2008). Tail reconnection triggering substorm onset. *Science*, *321*, 931–935.

Arnold, H., Swisdak, M., & Drake, J. F. (2018). Characterizing ion flows across a magnetotail dipolarization jet. *Journal of Geophysical Research: Space Physics*, *123*, 6326–6334. https://doi.org/10.1029/2018JA025604

Baker, D. N., Hones, E. W. J., Young, D. T., & Birn, J. (1982). The possible role of ionospheric oxygen in the initiation and development of plasma sheet instabilities. *Geophysical Research Letters*, *9*, 1337–1340.

Birn, J., Drake, J. F., Shay, M. A., Rogers, B. N., Denton, R. E., Hesse, M., et al. (2001). Geospace Environmental Modeling (GEM) magnetic reconnection challenge. *Journal of Geophysical Research*, *106*(A3), 3715–3719.

Bowers, K. J., Albright, B. J., Bergen, B., Yin, L., Barker, K. J., & Kerbyson, D. J. (2008). 0.374 pflop/s trillion-particle kinetic modeling of laser plasma interaction on roadrunner. In *Proceedings of the 2008 ACM/IEEE Conference on Supercomputing* (pp. 63). IEEE Press

Bowers, K. J., Albright, B. J., Yin, L., Bergen, B., & Kwan, T. J. T. (2008). Ultrahigh performance three-dimensional electromagnetic relativistic kinetic plasma simulation. *Physics of Plasmas*, *15*(5), 055,703.

Bowers, K. J., Albright, B. J., Yin, L., Daughton, W., Roytershteyn, V., Bergen, B., & Kwan, T. J. T. (2009). Advances in petascale kinetic plasma simulation with VPIC and roadrunner. In *Journal of Physics: Conference Series*, (Vol. 180, pp. 012055). IOP Publishing.

Cassak, P. A., Liu, Y.-H., & Shay, M. A. (2017). A review of the 0.1 reconnection rate problem. *Journal of Plasma Physics*, *83*, 715830501.

Chen, Y., Toth, G., Jia, X., Slavin, J., Sun, W., Markidis, S., et al. (2019). Studying dawn-dusk asymmetries of Mercury's magnetotail using MHD-EPIC simulations. *Journal of Geophysical Research: Space Physics*, *124*, 8954–8973. https://doi.org/10.1029/2019JA026840

Daughton, W., Roytershteyn, V., Karimabadi, H., Yin, L., Albright, B. J., Bergen, B., & Bowers, K. J. (2011). Role of electron physics in the development of turbulent magnetic reconnection in collisionless plasmas. *Nature Physics*, *7*(7), 539.

Dong, C., Wang, L., Hakim, A., Bhattacharjee, A., Slavin, J. A., DiBraccio, G. A., & Germaschewski, K. (2019). A novel ten-moment multifluid model for Mercury: From the planetary conducting core to the dynamic magnetosphere. *Geophysical Research Letters*, *46*, 11,584–11,596. https://doi.org/10.1029/2019GL083180

Dorelli, J. C., Glocer, A., Collinson, G., & Tóth, G. (2015). The role of the hall effect in the global structure and dynamics of planetary magnetospheres: Ganymede as a case study. *Journal of Geophysical Research: Space Physics*, *120*, 5377–5392. https://doi.org/10.1002/2014JA020951

Drake, J. F., Swisdak, M., Phan, T. D., Cassak, P. A., Shay, M. A., Lepri, S. T., et al. (2009). Ion heating resulting from pickup in magnetic reconnection exhausts. *Journal of Geophysical Research*, *114*, A05111. https://doi.org/10.1029/2008JA013701

Dungey, J. (1961). Interplanetary magnetic field and the auroral zones. *Physical Review Letters*, *6*(2), 47–48.

Genestreti, K. J., Varsani, A., Burch, J. L., & Cassak, P. A. (2018). MMS observation of asymmetric reconnection supported by 3-D electron pressure divergence. *Geophysical Research Letters*, *123*, 1806–1821. https://doi.org/10.1002/2017JA025019

Giovanelli, R. G. (1946). A theory of chromospheric flares. *Nature*, *158*(4003), 81.

Gosling, J. T., Skoug, R. M., McComas, D. J., & Smith, C. W. (2005). Direct evidence for magnetic reconnection in the solar wind near 1 AU. *Journal of Geophysical Research*, *110*, A01107. https://doi.org/10.1029/2004JA010809

Huang, K., Lu, Q., Gao, L., Ji, H., Wang, X., & Fan, F. (2018). Particle-in-cell simulations of magnetically driven reconnection using laser-powered capacitor coils. *Physics of Plasmas*, *25*(5), 052,104.

Huang, C., Lu, Q., Yang, Z., Wu, M., Dong, Q., & Wang, S. (2011). The evolution of electron current sheet and formation of secondary islands in guide field reconnection. *Nonlinear Processes in Geophysics*, *18*(5), 727–733.

Ji, H., Yamada, M., Hsu, S., & Kulsrud, R. (1998). Experimental test of the sweet-parker model of magnetic reconnection. *Physical Review Letters*, *80*(15), 3256.

Li, T. C., Liu, Y.-H., Hesse, M., & Zou, Y. (2020). Three-dimensional x-line spreading in asymmetric magnetic reconnection. *Journal of Geophysical Research: Space Physics*, *125*, e2019JA027094. https://doi.org/10.1029/2019JA027094

Liu, J., Angelopoulos, V., Zhou, X.-Z., Yao, Z.-H., & Runov, A. (2015). Cross-tail expansion of dipolarizing flux bundles. *Journal of Geophysical Research: Space Physics*, *120*, 2516–2530. https://doi.org/10.1002/2015JA020997

Liu, Y.-H., Daughton, W., Karimabadi, H., Li, H., & Roytershteyn, V. (2013). Bifurcated structure of the electron diffusion region in three-dimensional magnetic reconnection. *Physical Review Letters*, *110*, 265,004.

Liu, Y.-H., & Hesse, M. (2016). Suppression of collisionless magnetic reconnection in asymmetric current sheets. *Physical of Plasmas*, *23*, 060,704.

Liu, Y.-H., Hesse, M., Guo, F., Daughton, W., Li, H., Cassak, P. A., & Shay, M. A. (2017). Why does steady-state magnetic reconnection have a maximum local rate of order 0.1? *Physical Review Letters*, *118*, 085,101.

Liu, Y.-H., Hesse, M., Li, T. C., Kuznetsova, M., & Le, A. (2018). Orientation and stability of asymmetric magnetic reconnection x line. *Journal of Geophysical Research: Space Physics*, *123*, 4908–4920. https://doi.org/10.1029/2018JA025410

Liu, Y.-H., Li, T. C., Hesse, M., Sun, W. J., Liu, J., Burch, J., et al. (2019). Three-dimensional magnetic reconnection with a spatially confined x-line extent: Implications for dipolarizing flux bundles and the dawn-dusk asymmetry. *Journal of Geophysical Research: Space Physics*, *124*, 2819–2830. https://doi.org/10.1029/2019JA026539

Lu, Q., Wang, H., Wang, X., Lu, S., Wang, R., Gao, X., & Wang, S. (2020). Turbulence-driven magnetic reconnection in the magnetosheath downstream of a quasi-parallel shock: A three-dimensional global hybrid simulation. *Geophysical Research Letters*, *47*, e2019GL085661. https://doi.org/10.1029/2019GL085661

Masuda, S., Kosugi, T., Hara, H., Tsuneta, S., & Ogawara, Y. (1994). A loop-top hard X-ray source in a compact solar flare as evidence for magnetic reconnection. *Nature*, *371*, 495.

Meyer, J. C. (2015). Structure of the diffusion region in three dimensional magnetic reconnection (Ph.D. Thesis), University of Delaware.

Nagai, T., Shinohara, I., Zenitani, S., Nakamura, R., Nakamura, T. K. M., Fujimoto, M., et al. (2013). Three-dimensional structure of magnetic reconnection in the magneotail from geotail observations. *Journal of Geophysical Research: Space Physics*, *118*, 1667–1678. https://doi.org/10.1029/1667-1678

Nakamura, R., Baumjohann, W., Mouikis, C., Kistler, L. M., Runov, A., Volwerk, M., et al. (2004). Spatial scale of high-speed flows in the plasma sheet observed by Cluster. *Geophysical Research Letters*, *31*, L09804. https://doi.org/10.1029/2004GL019558

Nakamura, T. K. M., Genestreti, K. J., Liu, Y. H., Nakamura, R., Teh, W. L., Hasegawa, H., et al. (2018). Measurement of the magnetic reconnection rate in Earth's magnetotail. *Journal of Geophysical Research: Space Physics*, *123*, 9150–9168. https://doi.org/10.1029/2018JA025713

Nakamura, R., Genestreti, K. J., Nakamura, T. K. M., Baumjohann, W., & Varsani, A. T. N. (2018). Structure of the current sheet in the 2017/07/11 electron diffusion region event. *Journal of Geophysical Research: Space Physics*, *123*, 1173–1186. https://doi.org/10.1029/2018JA026028

Nakamura, T. K. M., Nakamura, R., Alexandrova, A., Kubota, Y., & Nagai, T. (2012). Hall magnetohydrodynamic effects for three-dimensional magnetic reconnection with finite width along the direction of the current. *Journal of Geophysical Research*, *117*, A03220. https://doi.org/10.1029/2011JA017006

Nishimura, Y., & Lyons, L. R. (2016). Localized reconnection in the magnetotail driven by lobe flow channels: Global MHD simulation. *Journal of Geophysical Research: Space Physics*, *121*, 1327–1338. https://doi.org/10.1002/2015JA022128

Olson, J., Egedal, J., Greess, S., Myers, R., Clark, M., Endrizzi, D., et al. (2016). Experimental demonstration of the collisionless plasmoid instability below the ion kinetic scale during magnetic reconnection. *Physical review letters*, *116*(25), 255,001.

Parker, E. N. (1957). Sweet's mechanism for merging magnetic fields in conducting fluids. *Journal of Geophysical Research*, *62*(4), 509–520.

Phan, T. D., Gosling, J. T., Davis, M. S., Skoug, R. M., Øieroset, M., Lin, R. P., et al. (2006). A magnetic reconnection X-line extending more than 390 Earth radii in the solar wind. *Nature*, *439*, 175–178.

Pritchett, P. L., & Coroniti, F. V. (2011). Plasma sheet disruption by interchange-generated flow intrusions. *Geophysical Research Letters*, *38*, L10102. https://doi.org/10.1029/2011GL047527

Pritchett, P. L., Coroniti, F. V., & Nishimura, Y. (2014). The kinetic ballooning/interchange instability as a source of dipolarization fronts and auroral streamers. *Journal of Geophysical Research: Space Physics*, *119*, 4723–4739. https://doi.org/10.1002/2014JA019890

Rong, Z. J., Ding, Y., & Slavin, J. A. (2018). The magnetic field structure of mercury's magnetotail. *Journal of Geophysical Research: Space Physics*, *123*, 548–566. https://doi.org/10.1002/2017JA024923

Russell, C. T., Saunders, M. A., Phillips, J. L., & Fedder, J. A. (1986). Near-tail reconnection as the cause of cometary tail disconnections. *Journal of Geophysical Research*, *91*(A2), 1417–1423.

Shay, M. A., & Drake, J. F. (1998). The role of electron dissipation on the rate of collisionless magnetic reconnection. *Geophysical Research Letters*, *25*(20), 3759–3762.

Shay, M. A., Drake, J. F., Swisdak, M., Dorland, W., & Rogers, B. N. (2003). Inherently three dimensional magnetic reconnection: A mechanism for bursty bulk flows? *Geophysical Research Letters*, *30*, 1345.

Shepherd, L. S., & Cassak, P. A. (2012). Guide field dependence of 3-D x-line spreading during collisionless magnetic reconnection. *Journal of Geophysical Research*, *117*, A10101. https://doi.org/10.1029/2012JA017867

Slavin, J. A., Acuña, M. H., Anderson, B. J., Baker, D. N., Benna, M., Boardsen, S. A., et al. (2009). Messenger observations of magnetic reconnection in Mercury's magnetosphere. *Science*, *324*(5927), 606–610.

Sun, W. J., Fu, S. Y., Slavin, J. A., Raines, J. M., Zong, Q. G., Poh, G. K., & Zurbuchen, T. H. (2016). Spatial distribution of mercury's flux ropes and reconnection fronts: Messenger observations. *Journal of Geophysical Research: Space Physics*, *121*, 7590–7607. https://doi.org/10.1002/2016JA022787

Tobert, R. B., Burch, J. L., Phan, T. D., Hesse, M., & Argall, M. R. (2018). Electron-scale dynamics of the diffusion region during symmetric magnetic reconnection in space. *Science*, *362*, 1391.

Uzdensky, D. A. (2011). Magnetic reconnection in extreme astrophysical environments. *Space Science Reviews*, *160*(1–4), 45–71.

van Casteren, B. J., Hayakawa, J., Fujimoto, H., Laakso, M., & Novara, H. (2010). BepiColombo—Comprehensive exploration of Mercury: Mission overview and science goals. *Planetary and Space Science*, *58*, 2–20.

Wygant, J. R., Cattell, C. A., Lysak, R., Song, Y., Dombeck, J., McFadden, J., et al. (2005). Cluster observations of an intense normal component of the electric field at a thin reconnecting current sheet in the tail and its role in the shock-like acceleration of the ion fluid into the separatrix region. *Journal of Geophysical Research*, *110*, A09206. https://doi.org/10.1029/2004JA010708

Zou, Y., Walsh, B. M., Atz, E., Liang, H., & Angelopoulos, V. (2020). Azimuthal variation of magnetopause reconnection at scales below an earth radius. *Geophysical Research Letters*, *47*, e2019GL086500. https://doi.org/10.1029/2019GL086500

Zweibel, E. G., & Yamada, M. (2009). Magnetic reconnection in astrophysical and laboratory plasmas. *Annual Review of Astronomy and Astrophysics*, *47*, 291–332.